Tailoring Magnetic Exchange Interactions in Ferromagnet-Intercalated $MnBi_2Te_4$ Superlattices

Peng Chen[1,2,3†], Qi Yao[4,5†*], Junqi Xu[6], Qiang Sun[7,8], Alexander J. Grutter[9], P. Quarterman[9], Purnima P. Balakrishnan[9], Christy J. Kinane[10], Andrew J. Caruana[10], Sean Langridge[10], Ang Li[11], Barat Achinuq[12], Emily Heppell[12], Yuchen Ji[4,5], Shanshan Liu[13], Baoshan Cui[14,15], Jiuming Liu[1], Puyang Huang[1], Zhongkai Liu[4,5], Guoqiang Yu[14,15],Faxian Xiu[13], Thorsten Hesjedal[12], Jin Zou[7,8], Xiaodong Han[11], Haijun Zhang[6,16], Yumeng Yang[1*], and Xufeng Kou[1,4*]

[1]School of Information Science and Technology, ShanghaiTech University, Shanghai, 201210, China

[2]Shanghai Institute of Microsystem and Information Technology, Chinese Academy of Sciences, Shanghai 200050, China

[3]University of Chinese Academy of Science, Beijing 101408, China

[4]ShanghaiTech Laboratory for Topological Physics, ShanghaiTech University, Shanghai 201210, China

[5]School of Physical Science and Technology, ShanghaiTech University, Shanghai, 201210, China

[6]National Laboratory of Solid-State Microstructures, School of Physics, Nanjing University, Nanjing 210093, China

[7]School of Mechanical and Mining Engineering, The University of Queensland, QLD 4072, Australia

[8]Centre for Microscopy and Microanalysis, The University of Queensland, St Lucia, QLD 4072, Australia

[9]NIST Center for Neutron Research, National Institute of Standards and Technology, Gaithersburg, Maryland 20899-6102, USA

[10]ISIS-Neutron and Muon Source, Rutherford Appleton Laboratory, Didcot, OX11 0QX, United Kingdom

[11]Institute of Microstructure and Property of Advanced Materials, Beijing University of Technology, Beijing 100124, China

[12]Department of Physics, Clarendon Laboratory, University of Oxford, Parks Road, Oxford, OX1 3PU, UK

[13]State Key Laboratory of Surface Physics, Department of Physics, Fudan University, Shanghai 200433, China

[14]Songshan Lake Materials Laboratory Dongguan, Guangdong 523808, China

[15]Beijing National Laboratory for Condensed Matter Physics Institute of Physics Chinese Academy of Sciences Beijing 100190, China

[16]Collaborative Innovation Center of Advanced Microstructures, Nanjing University, Nanjing 210093, China

†These authors contributed equally to this work.

*Correspondence to: yaoqi@shanghaitech.edu.cn; yangym1@shanghaitech.edu.cn; kouxf@shanghaitech.edu.cn;

The intrinsic magnetic topological insulator $MnBi_2Te_4$ (MBT) has provided a platform for the successful realization of exotic quantum phenomena. To broaden the horizons of MBT-based material systems, we intercalate ferromagnetic MnTe layers to construct the $[(MBT)(MnTe)_m]_N$ superlattices by molecular beam epitaxy. The effective incorporation of the ferromagnetic spacer mediates the anti-ferromagnetic interlayer coupling among the MBT layers through the exchange spring effect at the MBT/MnTe hetero-interfaces. Moreover, the precise control of the MnTe thickness enables the modulation of relative strengths among the constituent magnetic orders, leading to tunable magneto-resistance responses, while the superlattice periodicity serves as an additional tuning parameter to tailor the spin configurations of the synthesized multi-layers. Our results demonstrate the advantages of superlattice engineering for optimizing the magnetic interactions in MBT-family systems, and the ferromagnet-intercalated strategy opens up new avenues in magnetic topological insulator structural design and spintronic applications.

In magnetic topological insulators (MTIs), the co-existence of broken time-reversal symmetry (TRS) and topologically non-trivial surface states gives rise to a variety of TRS-breaking physics[1-6]. So far, the most commonly-adopted method to obtain MTIs is the incorporation of transition-metal elements (Cr, V, Mn) into the host TI matrix to establish the robust ferromagnetism[2,7,8]. However, the random distribution of magnetic atoms inevitably leads to a spatial fluctuation of the magnetic exchange gap, which restricts MTI-related phenomena at deep cryogenic temperatures[9]. One feasible solution to address such challenge is the design of the TI-based magnetic heterostructures in which uniform magnetic order can be induced via the interfacial proximity effect[10,11]. In this way, the separation of the topology and the magnetism into different layers allows us to control their contributions independently. However, due to critical lattice-matching requirements, the selection of TI-compatible magnetic films is limited and only a few MTI heterostructures have been fabricated[11-13].

Alternatively, $MnBi_2Te_4$ (MBT), an intrinsic MTI material, has aroused extensive attention in recent

years[14-16]. In contrast to magnetic doping, the covalently-bonded Mn atoms strictly form a two-dimensional lattice plane within the stacked Te-Bi-Te-Mn-Te-Bi-Te septuple layers (SL)[17,18]. This SL structure not only preserves the large spin-orbit coupling (SOC) required for band inversion, but also provides a homogeneous magnetic ground-state with intra-layer ferromagnetism (FM) and interlayer A-type anti-ferromagnetism (AFM)[17]. As a result, dissipationless chiral edge conduction has been observed in thin MBT flakes above 1 K, although it requires the presence of a large external magnetic field to fully magnetize the samples[14,19,20].

In this context, new breakthroughs may emerge through deliberate modifications of the MBT framework, from which spontaneous magnetization can be achieved at zero magnetic field[14]. For instance, recent attempts by inserting the Bi_2Te_3 spacer in the (MBT)$(Bi_2Te_3)_n$ (n = 1-6)-series crystals have been made, where the interlayer AFM-type Anderson super-exchange coupling strength is reduced significantly with increasing of n[21-25], and this non-magnetic intercalation strategy may cause unintended magnetic fluctuations[26]. Instead, the $Mn_2Bi_2Te_5$ system has been proposed as a superior candidate given that the additional Mn layer in the Mn-Te double spacer improves the magnetic stability of the original MBT SL. Unfortunately, during the $Mn_2Bi_2Te_5$ single crystal growth, the Mn atoms tend to dope into MBT rather than forming the stable Mn-Te-Mn structure[17], and the experimental realization of FM-intercalated MBT proposals remains elusive[27].

In this work, we utilize the molecular beam epitaxy (MBE) technique to integrate ferromagnetic MnTe and MBT into $[(MBT)(MnTe)_m]_N$ superlattices, where m is the nominal MnTe layer coverage, N is the number of superlattice periods, and the thickness of the MBT is fixed as one septuple layer within each period for direct comparisons. The insertion of the MnTe spacer with perpendicular FM order excels in both tuning the AFM-to-FM strength and stabilizing the interlayer exchange coupling between MBT layers. Furthermore, through deliberate superlattice periodicity control, we also manipulate the spin texture of the entire superlattice structure with configurable magneto-resistance (MR) responses. The generic design rules of FM/MBT hybrid systems may shed light on the exploration of MTI-based physics and multi-functional device applications.

Structural and magnetic properties of MBT and $[(MBT)(MnTe)_m]_N$ samples. We first grew MBT thin films by depositing individual MnTe and Bi_2Te_3 layers on 2-inch Al_2O_3(0001) substrates in an alternating sequence, followed by a moderate post-annealing procedure to form the MBT SL structure. The absence of dangling bonds on the Al_2O_3 surface promotes the epitaxial growth of MBT, and the sharp streaky pattern of

the *in-situ* reflection high-energy electron diffraction (RHEED) reveals the two-dimensional growth mode of the as-grown MBT films (Fig. 1a). The cross-sectional high-resolution scanning transmission electron microscopy (HR-STEM) image of the MBT sample (Fig. 1b) clearly unveils the highly ordered atomic distribution of the desired Te-Bi-Te-Mn-Te-Bi-Te sequence. In addition, the quantitative analysis of the intensity distribution in Fig. 1c confirms an elemental composition ratio of Mn: Bi: Te = 1: 2: 4 in the single-crystalline thin film, and the X-ray diffraction (XRD) pattern (Supplementary Fig. 1) exhibits a series of (00*n*) peaks without observable secondary phases, both of which agree well with the ideal stoichiometric MBT values. Additionally, through the polarized neutron reflectometry (PNR) measurements of the Te-capped MBT film, the nuclear scattering length density (SLD) profile is consistent with the bulk MBT spectrum, and the magnetic SLD diagram shows a uniform magnetization distribution across the film, with a magnitude in accordance with that expected from MBT in an in-plane magnetic field, supporting high-quality growth of the designed phase (Supplementary Fig. 2-1).

Subsequently, we performed six-point magneto-transport experiments on the 5 SL MBT sample to explore its magnetic/electrical properties. Consistent with studies of exfoliated MBT flakes[14,19,28], the magneto-resistance displays a hump-like line-shape at T = 1.5 K, as highlighted in Fig. 1d. In particular, the initial anti-parallel alignment of spins in adjacent MBT layers leads to the high-MR state in the low-magnetic-field region, and the abrupt increase in magnitude to a MR peak near a field of ± 3.3 T (*i.e.,* defined as the transition field H_t) corresponds to the characteristic spin-flop feature for an *A*-type AFM system[14,19,28]. Upon further increasing the applied magnetic field, all magnetic moments become polarized along the *z*-direction at the saturation field of H_s = 7 T, and the MBT sample falls into a low-MR state. This behavior is similar to the giant magnetoresistance (GMR) effect found in a spin-valve system (the detailed GMR model is discussed in Supplementary Fig. 3). Besides, as long as the Mn:Bi:Te element ratio is accurately tuned, the corresponding anomalous Hall resistance (R_{xy}) (Fig. 1e) reaches its saturation value of R_s = 4 kΩ, which is higher than the Bi_2Te_3-excess and MnTe-excess MBT counterparts (see Supplementary Fig. 4). It is noted that the hybrid-AHE-like R_{xy} slope at low magnetic fields (± 3.3 T) may be caused by native anti-site defects and/or random stacking order in MBT, which in turn modify the local electronic structures and magnetic moments[25,27,29]. From the aforementioned structural and electrical characterizations, we have validated the high quality of our MBT layer as a reliable building block for the following study.

Based on our previous experience with the FM-phase MnTe film growth[30], we have chosen it as the intercalated layer to create the $[(MBT)(MnTe)_m]_N$ system. As illustrated in Fig. 1f, by carefully choosing the

appropriate substrate temperature window and a moderate post-annealing process (Methods), the similar 2D stoichiometric structures with a negligible lattice mismatch between the FM-phase α-MnTe and MBT guarantees the epitaxial growth of the superlattice structure in which the strong perpendicular ferromagnetism (*i.e.,* Curie temperature of T_C ~ 150 K) of MnTe can add robust FM interactions to the hybrid system (Supplementary Fig. 5), and the surface coverage of the MnTe spacer between adjacent MBT layers m (*i.e.*, which statistically equals to the total growth time of the MnTe layer divided by that of one MnTe unit cell) can be, in principle, utilized to tune the interlayer AFM coupling[31,32]. It is noteworthy that the maximum thickness of the MnTe layer in this study is limited below 1.34 nm (*i.e.,* 2 MnTe layers), which is sufficiently thin to ensure effective couplings among MBT layers in the superlattice[26,33].

Given the known tendency of Mn to diffuse extensively in MBT-related systems, we further performed neutron reflectometry experiments to directly probe the depth-resolved magnetization profiles in the $[(MBT)(MnTe)_m]_N$ superlattices. Firstly, an unpolarized measurement of the nominal m = 1.75 sample with N = 10 superlattice repeats yields an experimental MnTe layer coverage of m = 1.72, well within the experimental uncertainty of the expected value (Supplementary Fig. 2-2). Together with the appearance of the anticipated superlattice first order Bragg reflection peak at a very high reciprocal lattice vector of $Q \approx 2.7$ nm^{-1}, such supplementary information certifies the realization of large-area, highly periodic $[(MBT)(MnTe)_{1.75}]_{10}$ structure by MBE (Supplementary Fig. 2-2a). Next, an additional PNR measurement was conducted at T = 6 K under the applied in-plane magnetic field of 3 T. Figures 2a-b summarize the best fitting results of the non-spin-flip reflectivity and spin asymmetry signals (*i.e.,* defined as the difference between the spin-dependent reflectivities normalized by their sum) in reference to the desired $[(MBT)(MnTe)_{1.75}]_{10}$ superlattice structure. While the measurement did not reach the first order Bragg reflection due to the lower intensity of the polarized neutron beam, the oscillatory SLD depth profile in Fig. 2c is in line with the periodic superlattice formation, and its average amplitude resides within the reasonable range between the bulk MBT and MnTe values. Moreover, compared with the pure 6 SL MBT data (Supplementary Fig. S2-1c), the integrated magnetic moment of the $[(MBT)(MnTe)_{1.75}]_{10}$ sample detected by PNR manifests a net contribution to the magnetization from the incorporated MnTe layers. Assuming that the magnetic moment from each constituent layer itself does not increase progressively with the applied in-plane field, our PNR results thus indicate the resulting canted spin configuration with a non-zero in-plane magnetization of 30 emu/cc (*i.e.,* noting that this value is higher than that expected from the MnTe layer alone[34]) may originate from the interplay between the MBT and MnTe layers through interfacial and interlayer

exchange interactions.

Interlayer coupling mediated by the MnTe intercalation. In order to investigate the influence of MnTe intercalation, we have conducted the temperature-dependent MR measurements on a set of $[(MBT)(MnTe)_m]_5$ samples with m varying from 0 to 1.75 in Fig. 3. When the samples are cooled to T = 1.5 K (below the Néel temperature of MBT T_N = 25 K[16]), the MR signals exhibit a strong m-dependence. As disclosed in Fig. 3a, the MR peak transition field H_t monotonically shrinks with the increase of the MnTe thickness (*i.e.,* the change of H_t compared to the pure FM-phase MnTe film (ΔH_t) successively reduces from 2.6 T (m = 0.25) to 0.5 T (m = 1.75) at T = 1.5 K, as marked by the red circles in Fig. 3c), signifying the effective modulation of the exchange-spring effect through the MnTe intercalation. Meanwhile, the dramatic decrease of the MR amplitude from m = 0 (12.5%) to m = 0.5 (2.65%) implies the suppression of the AFM-related GMR component by the introduced FM order. By further increasing m, the contribution of the MnTe layer becomes more pronounced, therefore triggering the appearance of a double-split butterfly MR response from its original curve. Eventually, the overall MR profiles of the MnTe-dominated superlattice system ($m \geq 0.75$) resembles that of the pure MnTe control sample except for a larger transition field (H_t). In fact, similar exchange-spring magnet-like MR behaviors are also observed in conventional magnetic multilayers (e.g., NiFe/IrMn and NiFe/Co stacks)[32,35]. Depending on the relative strengths of the anisotropy and exchange coupling energy between the magnetic components, the ground-state spin-texture of the system and its correlated magneto-transport responses can be tuned[31,36]. In our MnTe-intercalated MBT superlattices, when the soft magnet MnTe couples with the magnetically hard MBT single layer, the strong anisotropy of the latter can pin the magnetic moment within the MnTe layer via the magnetic proximity coupling at the interface[37-41], resulting in the enlarged transition field H_t. On the other hand, as the base temperature is elevated above the T_N of MBT, the absence of the AFM-type interlayer Anderson super-exchange coupling would drive the pure 5 SL MBT sample into a paramagnetic state, as verified by the positive, parabolic MR curve detected at 30 K (*i.e.,* the MBT curve of Fig. 3b). Afterwards, the entire magneto-transport behavior of the $[(MBT)(MnTe)_m]_5$ system is only governed by the remaining MnTe-related FM order. Consequently, typical butterfly-shape MR slopes with a constant peak position are recorded, regardless of the MnTe thickness (*i.e.,* same as the pure FM-type MnTe film[30]). Furthermore, relevant temperature-dependent H_t slopes in Fig. 3d display a clear MBT-to-MnTe transition trait as m varies from 0.25 to 1.75, providing a guidance in evaluating the competing intra-/inter-layer magnetic couplings.

In addition to enabling the coercivity modulation, the identified exchange-spring effect is found to stabilize the interlayer coupling between adjacent MBT layers in our $[(MBT)(MnTe)_m]_N$ superlattices. Unlike the m-dependent H_t phenomenon noted in the low-field region, the saturation field H_s, which characterizes the interlayer exchange coupling strength, remains constant at 7 T (*i.e.,* the same value as the non-intercalated MBT film) and shows a negligible variation with respect to m (*i.e.,* the dashed straight line in Fig. 3a). In order to understand this distinctive feature, we carried out high-field anomalous Hall resistance measurements on the same set of $[(MBT)(MnTe)_m]_5$ samples at low temperatures. Strikingly, the normalized Hall resistance (*i.e.,* defined as R_{xy}/R_s) curves at T = 1.5 K (Fig. 4a) shows almost identical contours, indicating a universal transition process as the magnetic moments in the superlattice are gradually aligned by the applied field. In agreement with the MR results in Fig. 3, the saturation field H_s values extracted from the AHE data at T =1.5 K, 3 K, 5 K, and 10 K also stay independent on the MnTe spacer thickness (Fig. 4b). Likewise, the H_s–T slopes also follow the same temperature-scaling trace up to 25 K (Fig. 4c), above which the interlayer AFM order disappears (*i.e.,* H_s = 0) and the overall AHE signal reverts to that of a single-phase FM-driven R_{xy} hysteresis loop.

Modified linear chain model. Quantitatively, the distinct evolutions of H_t and H_s versus the MnTe thickness can be well described by a modified linear chain model[42-44], in which the magnetization of each constituent MBT and MnTe layer is considered as a 'macro spin'. As schematized in Fig. 5a, the magnetic interactions in the $[(MBT)(MnTe)_m]_N$ superlattice system consist of the exchange couplings between nearest-neighbored MBT-to-MBT, MnTe-to-MnTe, and MBT-to-MnTe layers, respectively. Accordingly, the total energy E_N of the system can be expressed as a function of the applied magnetic field $\boldsymbol{H}$ [42-44]

$$E_N\left(\boldsymbol{m}_i^{\mathrm{MBT}}, \boldsymbol{m}_i^{\mathrm{MnTe}}, \boldsymbol{H}\right) = \sum_{i=1}^{N-1}\Big[J_i^{\mathrm{MBT}}\boldsymbol{m}_i^{\mathrm{MBT}}\cdot\boldsymbol{m}_{i+1}^{\mathrm{MBT}} + J_i^{\mathrm{MnTe}}\boldsymbol{m}_i^{\mathrm{MnTe}}\cdot\boldsymbol{m}_{i+1}^{\mathrm{MnTe}} + \tilde{J}_i^{\mathrm{MBT}}\left(\boldsymbol{m}_i^{\mathrm{MBT}}\cdot\boldsymbol{m}_{i+1}^{\mathrm{MBT}}\right)^2$$

$$+ \tilde{J}_i^{\mathrm{MnTe}}\left(\boldsymbol{m}_i^{\mathrm{MnTe}}\cdot\boldsymbol{m}_{i+1}^{\mathrm{MnTe}}\right)^2\Big] - \sum_{i=1}^{N} J_i^{ex}\boldsymbol{m}_i^{\mathrm{MBT}}\cdot\boldsymbol{m}_i^{\mathrm{MnTe}}$$

$$- \sum_{i=1}^{N}\left[K_i^{\mathrm{MBT}}t_i^{\mathrm{MBT}}\left(\boldsymbol{m}_i^{\mathrm{MBT}}\cdot\boldsymbol{z}\right)^2 + K_i^{\mathrm{MnTe}}t_i^{\mathrm{MnTe}}\left(\boldsymbol{m}_i^{\mathrm{MnTe}}\cdot\boldsymbol{z}\right)^2\right]$$

$$- \textstyle\sum_{i=1}^{N}\left(M_i^{\mathrm{MBT}}t_i^{\mathrm{MBT}}\boldsymbol{m}_i^{\mathrm{MBT}} + M_i^{\mathrm{MnTe}}t_i^{\mathrm{MnTe}}\boldsymbol{m}_i^{\mathrm{MnTe}}\right)\cdot\boldsymbol{H} \qquad (1)$$

where J_i^{MBT} and $\tilde{J}_i^{\mathrm{MBT}}$ (J_i^{MnTe} and $\tilde{J}_i^{\mathrm{MnTe}}$) are the bilinear and biquadratic interlayer exchange coupling

constants between adjacent MBT (MnTe) layers, J_i^{ex} denotes the MBT/MnTe interfacial magnetic interaction, $K_i^{MBT}(K_i^{MnTe})$, t_i^{MBT} (t_i^{MnTe}), M_i^{MBT} (M_i^{MnTe}), $\boldsymbol{m}_i^{MBT}(\boldsymbol{m}_i^{MnTe})$ correspond to the uniaxial anisotropy constant, thickness, saturated magnetization, and the unit vector of magnetization direction of the *i*th MBT (MnTe) layer, respectively. The third term accounts for the anisotropy energy, and the fourth term represents the field-induced Zeeman energy from the uncompensated moments. Under the exchange-spring interaction scenario, the intercalated MnTe acts as a soft FM mediating adjacent antiparallel-coupled MBT layers, and the impact of the i^{th} MnTe spacer on the MBT pair (M_i^{MBT} and M_{i+1}^{MBT}) can be expressed as the modifications of the effective interlayer exchange coupling (J_{eff}^{MBT}) and uniaxial anisotropy (K_{eff}^{MBT})[42]. Therefore, Equation (1) can be further expressed as the simplified formula:

$$E = J_{eff}^{MBT}[cos(\theta_i - \theta_{i+1}) + \beta\, cos^2(\theta_i - \theta_{i+1})] + K_{eff}^{MBT} t_i^{MBT}\left(sin^2\theta_i + \xi sin^2\theta_{i+1}\right)$$

$$- H_z t_i^{MBT}\left(M_i^{MBT} cos\theta_i + M_{i+1}^{MBT} cos\theta_{i+1}\right) \quad (2)$$

where θ_i (θ_{i+1}) is the angle deviation between $M_i^{MBT}(M_{i+1}^{MBT})$ and the magnetic easy-axis (*i.e.,* z-direction), β and ξ are introduced as the scaling factors of the biquadratic coupling and different anisotropy, and t_i^{MBT} is the MBT layer thickness (see Supplementary Information Section 6 for detailed discussion). From this modified linear chain model, it is found that the transition field H_t is affected by the K_{eff}^{MBT} value whereas the saturation field H_s is mainly decided by the J_{eff}^{MBT} magnitude (Supplementary Fig. 6). Consequently, to re-capture the *m*-dependent MR behaviors observed in Fig. 3, our simulation results suggest that on one hand, the insertion of MnTe modulates the magnetic orientation and anisotropy of the MBT layer (*i.e.,* intra-layer MBT coupling), and the calculated ground-state magnetic configuration of the superlattice with canted spin-polarization (right panel of Fig. 5a) is consistent with the PNR data elucidated in Fig. 2 (*i.e.,* the reduction of the effective anisotropy energy K_{eff}^{MBT} caused by MnTe insertion is also justified by the density functional theory calculation as discussed in Supplementary Information S7). On the other hand, the presence of MnTe-to-MnTe interlayer coupling and induced MnTe/MBT interfacial interaction both help to preserve the effective interlayer MBT coupling strength (*i.e.,* $J_{eff}^{MBT} = f(J_i^{MnTe}, J_i^{MBT}, J_i^{ex})$) with constant H_s and T_N via the exchange spring effect (Supplementary Fig. 8 and Fig. 9)[31,45,46]. Here, we should point out that once the MnTe spacer is replaced by a non-magnetic layer (*e.g.,* $(Bi_{1-x}Sb_x)_2Te_3$, BST), the FM-associated exchange interactions are absent in the resulting $[(MBT)(BST)_1]_N$ counterpart (*i.e.,* confirmed by magneto-transport and X-ray magnetic circular dichroism data of in Supplementary Figs. 10 and Fig. 11), leaving the interlayer MBT coupling determined exclusively by the Anderson super-exchange mechanism (*i.e.,* $J_{eff}^{MBT} = J_i^{MBT}$). Guided

by the same underlying physics elaborated in the modified linear-chain model, it has been reported in the (MBT)(Bi_2Te_3)$_n$ system, the negative correlation between the AFM-type J_i^{MBT} and the intercalation distance would also result in a rapid suppression of T_N and reduction of H_s with increasing n[20,22].

Tuning the interlayer coupling by superlattice engineering. Finally, we show the manipulation of the magnetic/spin configuration in the [(MBT)($MnTe$)$_m$]$_N$ system through superlattice structural engineering. In pure MBT thin films, since both the intra-layer FM and interlayer AFM strength are non-adjustable with the fixed crystalline structure, Fig. 5b shows that the overall MR profile always maintains the GMR-like line-shape with slightly enlarged H_t and H_s fields as the MBT thickness varies from the 2D (4 SL) to quasi-3D (10 SL) region (the sample thicknesses are calibrated by X-ray reflectivity (XRR) in Supplementary Fig. 12 and Table 12). The reduced GMR amplitude is possibly caused by the increased bulk conduction in thicker films[14,19]. On the contrary, with the insertion of the MnTe spacer, the magnetic proximity effect can re-orient the magnetic moments at the MBT/MnTe interface[40,41,47]. Under such circumstance, it is expected that a change in the number of superlattice repeats (*i.e.,* the number of hetero-interfaces) will introduce dimension-dependent features into the related magneto-transport results. Specifically, the emerging butterfly-type double-split MR curve in the thin [(MBT)($MnTe$)$_{1.75}$]$_4$ sample with H_t = 2.5 T suggests the existence of a sizable FM moment that is comparable with the original AFM order in the MBT/MnTe/MBT/MnTe unit, similar to other FM/AFM multi-layer systems[48-50]. As the repeat number increases, the added J_i^{ex} at the hetero-interfaces would promote the exchange-spring effect, as emphasized by the enlarged H_t field in Fig. 5c. Given that the adjacent MBT coupling is mediated through the sandwiched MnTe layer, the increase of superlattice repeats will cement such long-range interactions and stabilize the new ground state. Along with the reinforced canted magnetization orientation which modifies the interfacial spin scattering, it is therefore unsurprising that a more prominent AFM-type GMR behavior is obtained in the N = 10 sample[10,51].

Discussion

In conclusion, we have demonstrated that combining ferromagnets with MBT facilitates the construction of intrinsic MTIs with configurable electronic structures and magnetic properties. In the FM-intercalated MBT systems, the versatile interfacial and interlayer magnetic exchange interactions offer an effective approach to shape the overall spin texture, and the AFM-to-FM transition can be well-controlled by structural engineering.

Unlike the $(MBT)(Bi_2Te_3)_n$ compounds, the insertion of the MnTe spacer triggers the exchange spring effect which plays an indispensable role in the preservation of the global AFM coupling between adjacent MBT layers throughout the superlattice structures, and this advantage endows the system to be robust against external perturbation, which is favorable for device stability considerations. More importantly, the MR responses can also be tailored via superlattice periodicity optimization, thus providing another degree of freedom in the design of practical spintronic memory/sensor prototypes over traditional magnetic multilayers. With the further exploration of exotic topological features embedded in the host MBT matrix, the $[(MBT)(MnTe)_m]_N$ may serve as an advanced platform for realizing axion insulator states and MTI-based exotic quantum phenomena.

Methods

Sample Fabrication and Structural Characterizations: The $[(MBT)(MnTe)_m]_N$ superlattice films were grown on the $Al_2O_3(0001)$ substrate by MBE under a vacuum level of 1×10^{-8} Pa. Prior to the sample growth, the Al_2O_3 substrate was pre-annealed at 570 °C in order to remove the absorbed contamination. During the MBE growth, high-purity Mn and Bi atoms were evaporated from standard Knudsen cells, while Te was evaporated by a thermal cracker cell. The epitaxial growth of one septuple $MnBi_2Te_4$ was achieved by the alternant deposition of one monolayer of Bi_2Te_3 and MnTe (*i.e.,* with the substrate temperatures of 200 °C and 370 °C, respectively), followed by a moderate post-annealing at 390 °C for 3 minutes. In order to ensure the single-crystallinity of MBT with the right Bi-Mn-Te ratio as well as the precise control of the MnTe coverage in the superlattice structures, the flux ratio of each element was quantified by the *in-situ* beam flux monitor. Meanwhile, the real-time growth condition and the as-grown surface atom configuration were monitored by the reciprocal RHEED patterns. Besides, X-ray diffraction and reflectivity were performed to verify the crystal structure and calibrate the film thickness, and atomic-resolution structural characterization was performed by aberration-corrected Hitachi HF5000 STEM/TEM under the high-angle annular dark field (HAADF) STEM mode, operated at 200 kV. Cross-section TEM specimen was prepared by FEI Scios FIB.

Transport Measurements: The as-grown superlattices were etched into a six-probe Hall bar geometry with a dimension of 2 mm × 1 mm. The electrodes were made by welding small pieces of indium onto the contact areas. The magneto-transport measurements of the fabricated devices were performed with the He^4 refrigerators (Oxford Teslatron PT system) where several experimental variables such as temperature,

magnetic field, and lock-in frequency were adjusted during the measurements. Multiple lock-in amplifiers and Keithley source meters (with an excitation AC current I = 1 μA) were connected to the samples so as to enable the precise four-point lock-in experiments.

Neutron Reflectometry: Unpolarized neutron reflectometry measurements and polarized neutron reflectometry measurements were performed using the PBR instrument at the NIST Center for neutron research. Incident and scattered neutrons were polarized parallel or antiparallel to the direction of the applied magnetic field. Due to the 3 T applied field, no net perpendicular magnetization is expected in the plane of the film, so that the spin-flip scattering cross-sections may be neglected. We consequently measured the non-spin-flip scattering cross-sections as a function of Q, the momentum transfer vector along the film normal direction. The data was reduced using the Reductus[52] software package. Further unpolarized neutron reflectometry measurements were performed using the POLREF[53] instrument at the ISIS Neutron and Muon Source[54]. The incident and scattered beams were unpolarized, and the reflectivity was measured at room-temperature, well above any magnetic transition. All reflectivity analysis was performed using the Refl1D software package[55].

First-principles calculations: The first-principle calculations were performed within the density functional theory (DFT) using the projector augmented-wave (PAW) method[56] as implemented in the Vienna ab initio simulation package (VASP)[57,58]. The exchange-correlation functional was treated under the generalized gradient approximation (GGA)[59], and the energy cutoff for the plane-wave basis was set to 420 eV for all calculations. The system geometry was optimized under full relaxation with a total energy tolerance 10^{-5} eV for both the bulk MBT and the $MBT(MnTe)_1$ intercalation compounds. The spin-orbit coupling effect was self-consistently included, and the 3*d*-orbitals of Mn atoms was considered by the DFT+U approach[60] introduced by Dudarev *et al.*[61] with U_{eff} = 5 eV for all results in this work. Besides, we used the optB86b-vdW functional proposed by Klimeš *et al.*[62] to describe the van der Waals interactions. Furthermore, in order to calculate different interlayer magnetic configurations, we constructed the 1×1×2 supercells for all systems. The magnetic exchange coupling parameters and single-ion anisotropy parameters of both bulk MBT and the $MBT(MnTe)_1$ were obtained using the Hamiltonian model proposed by Lado *et al.*[63].

***XMCD measurements*:** X-ray magnetic circular dichroism (XMCD) measurements were performed on beamline I10 (BLADE) at the Diamond Light Source (Oxfordshire, UK). X-ray absorption spectroscopy spectra were recorded at the Mn $L_{2,3}$ edges between 630 and 670 eV using surface-sensitive total electron yield (TEY) detection mode in an UHV environment (~10^{-10} mbar). The measurements were carried out in an

applied out-of-plane field of up to 7 T at various temperatures with the input x-rays under normal incidence. In addition, X-ray absorption spectroscopy spectra were recorded with right (σ^+) and left (σ^-) circularly polarized x-rays, and XMCD signals are obtained as their difference ($\sigma^+ - \sigma^-$).

Acknowledgements

This work is sponsored by the National Key R&D Program of China under the contract number 2017YFB0305400, National Natural Science Foundation of China (Grant No. 61874172 and 11904230), the Major Project of Shanghai Municipal Science and Technology (Grant No. 2018SHZDZX02), the Shanghai Engineering Research Center of Energy Efficient and Custom AI IC, and the Shanghaitech Quantum Device and Soft Matter Nano-fabrication Labs (SMN180827). X.F.K acknowledges the support from the Merck POC program and the Shanghai Rising-Star program (Grant No. 21QA1406000). Y.M.Y acknowledges the support from Shanghai Pujiang Program (Grant No. 20PJ1411500). The authors acknowledge the facilities, and the scientific and technical assistance, of the Australian Microscopy & Microanalysis Research Facility at the Centre for Microscopy and Microanalysis, The University of Queensland. Q.Y acknowledges the support from the Shanghai Sailing Program (Grant No. 19YF1433200). We would also like to thank the ISIS neutron facility for the awarding of beamtime RB2000244, DOI: 10.5286/ISIS.E.RB2000244. Certain commercial equipment is identified in this paper to foster understanding. Such identification does not imply recommendation or endorsement by NIST. Diamond Light Source is acknowledged for beamtime allocated on I10 under proposal MM30262. B.A. and T.H. acknowledge funding from the Engineering and Physical Sciences Research Council (EP/N032128/1).

Author contributions

X. F. Kou, and Q. Yao conceived and supervised the study. P. Chen grew the samples, performed the characterization measurements and conducted the transport measurements. Q. Yao and P. Chen analyzed the transport and characterization data. P. Chen and Y. M. Yang conducted the macro-spin simulations. J. Q. Xu and H. J. Zhang contributed the first-principle calculations. Q. Sun, A. Li, X. D. Han and J. Zou performed microscopy characterization. A. Grutter, P. Quarterman, P. P. Balakrishnan, C. Kinane, A. Caruana, and S. Langridge, performed the neutron reflectometry measurements. Barat Achinuq, Emily Heppell and Thorsten Hesjedal performed x-ray magnetic circular dichroism measurements. P. Chen, Q. Yao, Y. M. Yang and X. F.

Kou wrote the manuscript. All authors discussed the results and commented on the manuscript.

Competing financial interests

The authors declare no competing financial interests.

References

1 Chang, C. Z. *et al.* Experimental Observation of the Quantum Anomalous Hall Effect in a Magnetic Topological Insulator. *Science* **340**, 167-170 (2013).

2 Kou, X. *et al.* Scale-invariant quantum anomalous Hall effect in magnetic topological insulators beyond the two-dimensional limit. *Phys. Rev. Lett.* **113**, 137201 (2014).

3 Nomura, K. & Nagaosa, N. Surface-Quantized Anomalous Hall Current and the Magnetoelectric Effect in Magnetically Disordered Topological Insulators. *Phys. Rev. Lett.* **106**, 166802 (2011).

4 Li, R., Wang, J., Qi, X.-L. & Zhang, S.-C. Dynamical axion field in topological magnetic insulators. *Nat. Phys.* **6**, 284-288 (2010).

5 He, K., Wang, Y. & Xue, Q.-K. Quantum anomalous Hall effect. *Natl. Sci. Rev.* **1**, 38-48 (2013).

6 Tokura, Y., Yasuda, K. & Tsukazaki, A. Magnetic topological insulators. *Nat. Rev. Phys.* **1**, 126-143 (2019).

7 Kou, X. *et al.* Metal-to-insulator switching in quantum anomalous Hall states. *Nat. Commun.* **6**, 1-8 (2015).

8 Winnerlein, M. *et al.* Epitaxy and structural properties of $(V, Bi, Sb)_2Te_3$ layers exhibiting the quantum anomalous Hall effect. *Phys. Rev. Mater.* **1**, 011201 (2017).

9 Lee, I. *et al.* Imaging Dirac-mass disorder from magnetic dopant atoms in the ferromagnetic topological insulator $Cr_x(Bi_{0.1}Sb_{0.9})_{2-x}Te_3$. *Proc. Natl. Acad. Sci. U.S.A.* **112**, 1316-1321 (2015).

10 He, Q. L. *et al.* Tailoring exchange couplings in magnetic topological-insulator/antiferromagnet heterostructures. *Nat. Mater.* **16**, 94-100 (2017).

11 Katmis, F. *et al.* A high-temperature ferromagnetic topological insulating phase by proximity coupling. *Nature* **533**, 513-516 (2016).

12 Lang, M. *et al.* Proximity induced high-temperature magnetic order in topological insulator-ferrimagnetic insulator heterostructure. *Nano Lett.* **14**, 3459-3465 (2014).

13 Tang, C. *et al.* Above 400-K robust perpendicular ferromagnetic phase in a topological insulator. *Sci. Adv.* **3**, e1700307 (2017).

14 Deng, Y. *et al.* Quantum anomalous Hall effect in intrinsic magnetic topological insulator $MnBi_2Te_4$. *Science* **367**, 895-900 (2020).

15 Li, J. *et al.* Intrinsic magnetic topological insulators in van der Waals layered $MnBi_2Te_4$-family materials. *Sci. Adv.* **5**, eaaw5685 (2019).

16 Otrokov, M. M. *et al.* Prediction and observation of an antiferromagnetic topological insulator. *Nature* **576**, 416-422 (2019).

17 Gong, Y. *et al.* Experimental Realization of an Intrinsic Magnetic Topological Insulator. *Chin. Phys. Lett.* **36**, 076801 (2019).

18 Otrokov, M. M. *et al.* Highly-ordered wide bandgap materials for quantized anomalous Hall and magnetoelectric effects. *2D Mater.* **4**, 025082 (2017).

19 Liu, C. *et al.* Robust axion insulator and Chern insulator phases in a two-dimensional antiferromagnetic topological insulator. *Nat. Mater.* **19**, 522-527 (2020).

20 Yan, J.-Q. *et al.* A-type antiferromagnetic order in $MnBi_4Te_7$ and $MnBi_6Te_{10}$ single crystals. *Phys. Rev. Mater.* **4**, 054202 (2020).
21 Wu, J. *et al.* Toward 2D Magnets in the $(MnBi_2Te_4)(Bi_2Te_3)_n$ Bulk Crystal. *Adv. Mater.* **32**, 2001815 (2020).
22 Klimovskikh, I. I. *et al.* Tunable 3D/2D magnetism in the $(MnBi_2Te_4)(Bi_2Te_3)_m$ topological insulators family. *npj Quantum Mater.* **5**, 54 (2020).
23 Ding, L. *et al.* Crystal and magnetic structures of magnetic topological insulators $MnBi_2Te_4$ and $MnBi_4Te_7$. *Phys. Rev. B* **101**, 020412 (2020).
24 Vidal, R. C. *et al.* Topological Electronic Structure and Intrinsic Magnetization in $MnBi_4Te_7$: A Bi_2Te_3 Derivative with a Periodic Mn Sublattice. *Phys. Rev. X* **9**, 041065 (2019).
25 Shi, M. Z. *et al.* Magnetic and transport properties in the magnetic topological insulators $MnBi_2Te_4(Bi_2Te_3)_n$ (n = 1,2). *Phys. Rev. B* **100**, 155144 (2019).
26 He, K. & Xue, Q.-K. The Road to High-Temperature Quantum Anomalous Hall Effect in Magnetic Topological Insulators. *SPIN* **09**, 1940016 (2019).
27 Cao, L. *et al.* Growth and characterization of the dynamical axion insulator candidate $Mn_2Bi_2Te_5$ with intrinsic antiferromagnetism. *Phys. Rev. B* **104**, 054421 (2021).
28 Li, H. *et al.* Antiferromagnetic topological insulator $MnBi_2Te_4$: Synthesis and magnetic properties. *Phys. Chem. Chem. Phys.* **22**, 556-563 (2020).
29 Zhao, Y.-F. *et al.* Even–Odd Layer-Dependent Anomalous Hall Effect in Topological Magnet $MnBi_2Te_4$ Thin Films. *Nano Lett.* **21**, 7691-7698 (2021).
30 Chen, P. *et al.* Tailoring the hybrid anomalous Hall response in engineered magnetic topological insulator heterostructures. *Nano Lett.* **20**, 1731-1737 (2020).
31 Scholl, A., Liberati, M., Arenholz, E., Ohldag, H. & Stöhr, J. Creation of an antiferromagnetic exchange spring. *Phys. Rev. Lett.* **92**, 247201 (2004).
32 Park, B. G. *et al.* A spin-valve-like magnetoresistance of an antiferromagnet-based tunnel junction. *Nat. Mater.* **10**, 347-351 (2011).
33 He, K. $MnBi_2Te_4$-family intrinsic magnetic topological materials. *npj Quantum Mater.* **5**, 90 (2020).
34 Awana, G. *et al.* Critical analysis of proximity-induced magnetism in $MnTe/Bi_2Te_3$ heterostructures. *Phys. Rev. Mater.* **6**, 053402 (2022).
35 Boltaev, A., Pudonin, F., Sherstnev, I., Egorov, D. & Kozmin, A. Flat magnetic exchange springs as mechanism for additional magnetoresistance in magnetic nanoisland arrays. *J. Magn. Magn. Mater.* **428**, 132-135 (2017).
36 Nogués, J. & Schuller, I. K. Exchange bias. *J. Magn. Magn. Mater.* **192**, 203-232 (1999).
37 Hellwig, O., Kortright, J., Takano, K. & Fullerton, E. E. Switching behavior of Fe-Pt/Ni-Fe exchange-spring films studied by resonant soft-x-ray magneto-optical Kerr effect. *Phys. Rev. B* **62**, 11694 (2000).
38 Khan, M. Y., Shokr, Y. A. & Kuch, W. Coupling of pinned magnetic moments in an antiferromagnet to a ferromagnet and its role for exchange bias. *J. Phys.: Condens. Matter* **32**, 075801 (2019).
39 Chi, X. *et al.* Role of antiferromagnetic bulk exchange coupling on exchange-bias propagation. *Phys. Lett. A* **379**, 2772-2776 (2015).
40 Guo, S. *et al.* Influence of antiferromagnetic interlayer on the exchange coupling of FM1/AFM/FM2 multilayers. *J. Magn. Magn. Mater.* **344**, 35-38 (2013).
41 Bali, R. *et al.* Competing magnetic anisotropies in an antiferromagnet-ferromagnet-antiferromagnet trilayer. *J. Appl. Phys.* **106**, 113925 (2009).
42 Rößler, U. & Bogdanov, A. Magnetic phases and reorientation transitions in antiferromagnetically coupled multilayers. *Phys. Rev. B* **69**, 184420 (2004).
43 Wang, Z. *et al.* Determining the phase diagram of atomically thin layered antiferromagnet $CrCl_3$. *Nat.*

Nanotechnol. **14**, 1116-1122 (2019).
44 Yang, S. *et al.* Odd-Even Layer-Number Effect and Layer-Dependent Magnetic Phase Diagrams in $MnBi_2Te_4$. *Phys. Rev. X* **11**, 011003 (2021).
45 Kneller, E. F. & Hawig, R. The exchange-spring magnet: a new material principle for permanent magnets. *IEEE Trans. Magn.* **27**, 3588-3560 (1991).
46 Fullerton, E. E., Jiang, J. & Bader, S. Hard/soft magnetic heterostructures: model exchange-spring magnets. *J. Magn. Magn. Mater.* **200**, 392-404 (1999).
47 Gruyters, M. & Schmitz, D. Microscopic nature of ferro-and antiferromagnetic interface coupling of uncompensated magnetic moments in exchange bias systems. *Phys. Rev. Lett.* **100**, 077205 (2008).
48 Lu, J. *et al.* Design and Synthesis of an Artificial Perpendicular Hard Ferrimagnet with High Thermal and Magnetic Field Stabilities. *Sci. Rep.* **7**, 1-9 (2017).
49 Meng, L. *et al.* Anomalous thickness dependence of Curie temperature in air-stable two-dimensional ferromagnetic 1T-$CrTe_2$ grown by chemical vapor deposition. *Nat. Commun.* **12**, 1-8 (2021).
50 He, Y. *et al.* Large linear non-saturating magnetoresistance and high mobility in ferromagnetic MnBi. *Nat. Commun.* **12**, 1-7 (2021).
51 Butler, W., Zhang, X.-G., Nicholson, D. & MacLaren, J. Spin-dependent scattering and giant magnetoresistance. *J. Magn. Magn. Mater.* **151**, 354-362 (1995).
52 Maranville, B., Ratcliff, W. & Kienzle, P. Reductus: A stateless python data reduction service with a browser front end. *J. Appl. Crystallogr.* **51**, 1500-1506 (2018).
53 A. Grutter et al. *Mn-uniformity in Intrinsically Magnetic Topological Insulator Superlattices*, <https://doi.org/10.5286/ISIS.E.RB2000244> (2021).
54 *https://www.isis.stfc.ac.uk/Pages/polref.aspx*.
55 Kirby, B. J. *et al.* Phase-sensitive specular neutron reflectometry for imaging the nanometer scale composition depth profile of thin-film materials. *Curr. Opin. Colloid Interface* **17**, 44-53 (2012).
56 Blöchl, P. E. Projector augmented-wave method. *Phys. Rev. B* **50**, 17953 (1994).
57 Kresse, G. & Furthmüller, J. Efficient iterative schemes for ab initio total-energy calculations using a plane-wave basis set. *Phys. Rev. B* **54**, 11169 (1996).
58 Kresse, G. & Joubert, D. From ultrasoft pseudopotentials to the projector augmented-wave method. *Phys. Rev. B* **59**, 1758 (1999).
59 Perdew, J. P., Burke, K. & Ernzerhof, M. Generalized gradient approximation made simple. *Phys. Rev. Lett.* **77**, 3865 (1996).
60 Anisimov, V. I., Zaanen, J. & Andersen, O. K. Band theory and Mott insulators: Hubbard U instead of Stoner I. *Phys. Rev. B* **44**, 943 (1991).
61 Dudarev, S. L., Botton, G. A., Savrasov, S. Y., Humphreys, C. & Sutton, A. P. Electron-energy-loss spectra and the structural stability of nickel oxide: An LSDA+ U study. *Phys.Rev. B* **57**, 1505 (1998).
62 Klimeš, J., Bowler, D. R. & Michaelides, A. Van der Waals density functionals applied to solids. *Phys. Rev. B* **83**, 195131 (2011).
63 Lado, J. L. & Fernández-Rossier, J. On the origin of magnetic anisotropy in two dimensional CrI_3. *2D Mater.* **4**, 035002 (2017).

Figures

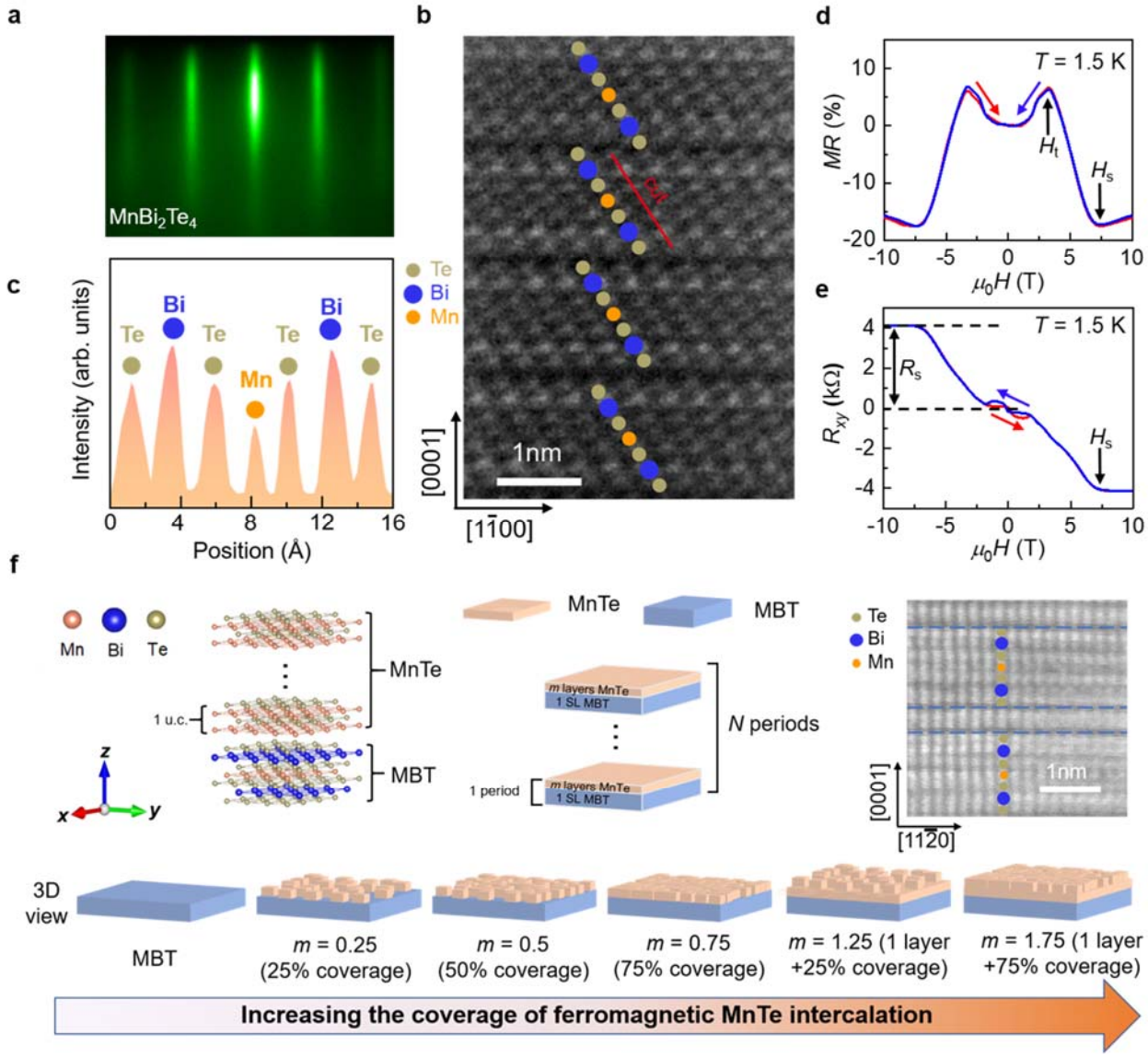

Figure 1. Structural and electrical characterizations of the MBE-grown MBT thin film. **a,** *In-situ* RHEED with a sharp streaky pattern reveals the epitaxial growth mode. **b,** Cross-sectional HR-STEM image of the MBT film grown on the Al_2O_3 (0001) substrate. **c,** Intensity distribution mapping along the cut marked in **b**. **d-e**, Magnetic field-dependent MR and R_{xy} data of the 5 SL MBT sample. Both the AFM-type GMR line-shape and spin-flop-induced hysteresis loop at 1.5 K are consistent with bulk MBT data. **f,** Schematic diagram of the FM-intercalated $[(MBT)(MnTe)_m]_N$ structure and the relevant HR-STEM image. By varying the intercalated MnTe layer coverage (m) and superlattice repeats (N), the magnetic exchange interactions can be regulated.

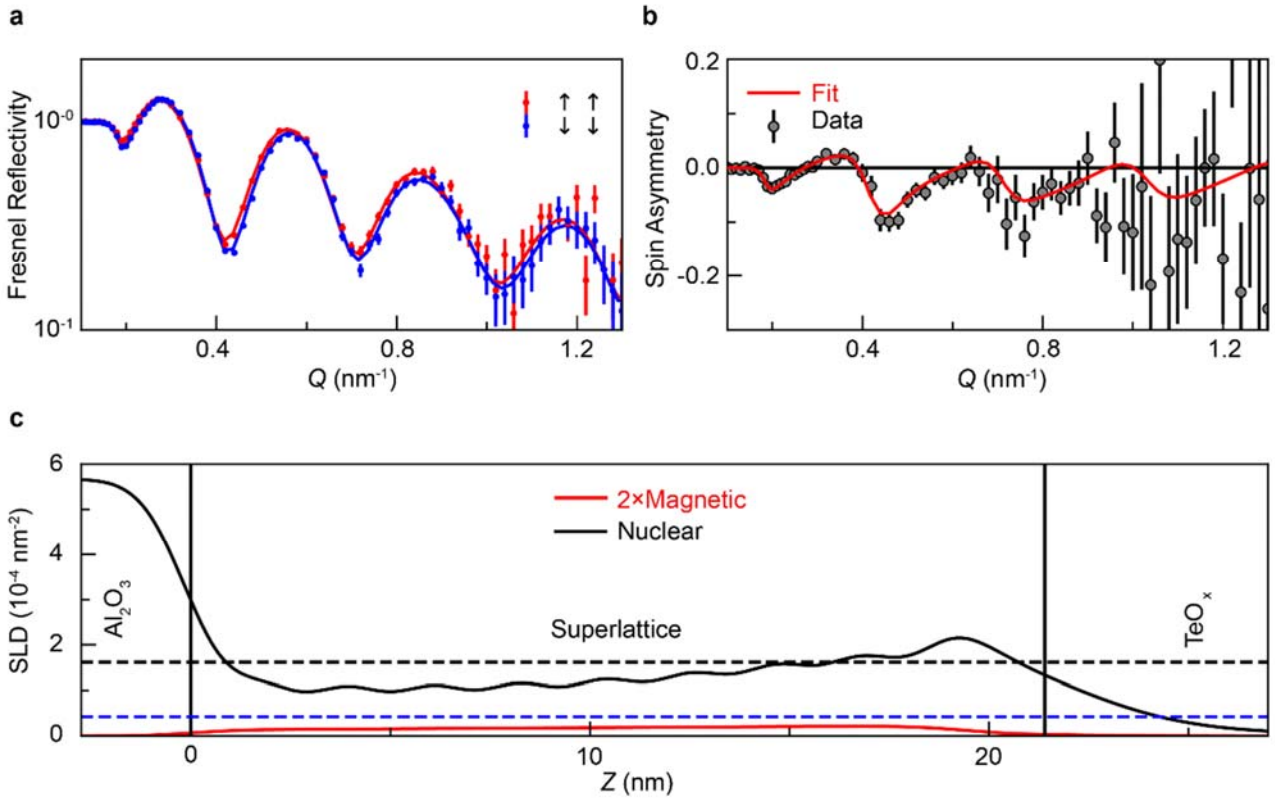

491

492 **Figure 2. Polarized neutron reflectometry measurements on the MBE-grown [(MBT)(MnTe)$_{1.75}$]$_{10}$**
493 **superlattice. a-b**, Polarized neutron reflectivity and spin asymmetry alongside best fit for the Te-capped
494 [(MBT)(MnTe)$_{1.75}$]$_{10}$ sample. **c**, Nuclear and magnetic scattering length density (SLD) profile used to generate
495 the fit. Error bars represent ±1 standard deviation. Measurements were performed at T = 6 K under a 3 T in-
496 plane applied magnetic field. The black dashed line represents the expected bulk nuclear SLD of the MBT
497 component while the blue dashed line corresponds to the ideal bulk nuclear SLD of MnTe. The depth-average
498 magnetization of around 30 emu/cc (averaged over the whole superlattice) is obtained from the PNR data.

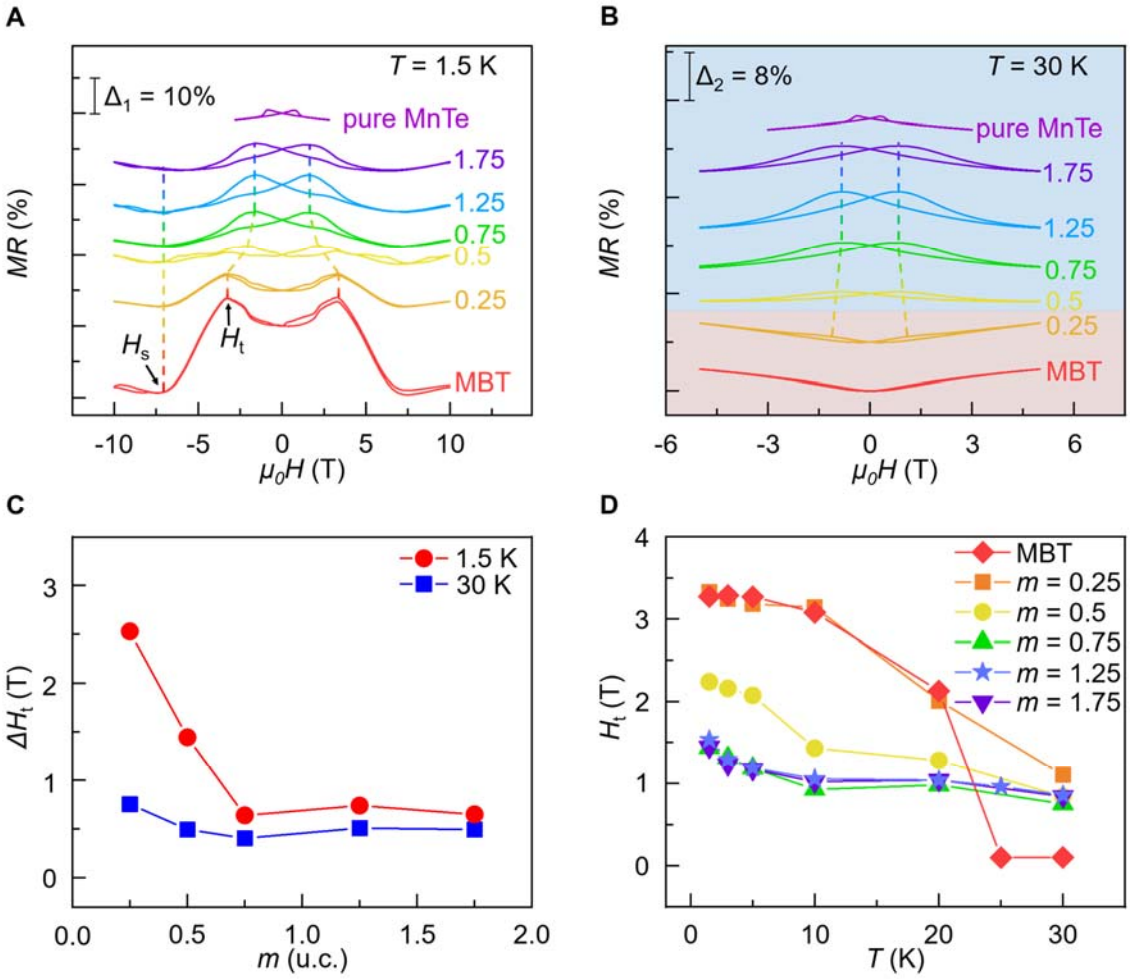

499

500 **Figure 3. Manipulation of the exchange spring effect in [(MBT)(MnTe)$_m$]$_5$ samples through MnTe**
501 **intercalation**. MnTe spacer thickness-dependent MR curves at **a,** T = 1.5 K and **b,** T = 30 K, respectively.
502 The value of m varies from 0 to 1.75. Data are shifted vertically by Δ_1 and Δ_2 for convenient comparison. **c,**
503 The evolutions of ΔH_t with respect to the MnTe thickness. The negative correlation between ΔH_t and m at 1.5
504 K (red circles) manifests the exchange spring effect whereas the constant ΔH_t values at 30 K (blue squares)
505 confirm the absence of the AFM order in the system above the Néel temperature. **d,** The temperature-
506 dependent H_t traces of the [(MBT)(MnTe)$_m$]$_5$ samples exhibit a clear MBT-to-MnTe transition feature at low
507 temperatures.

508

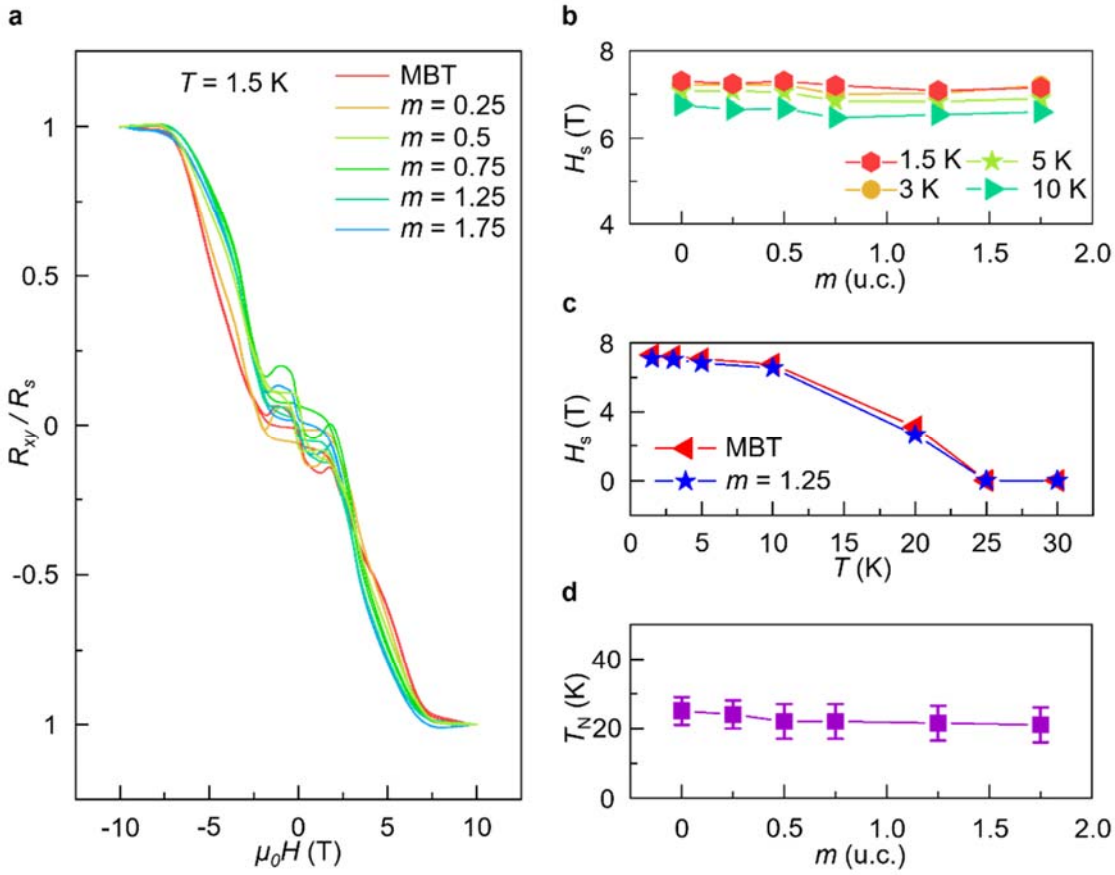

509

510 **Figure 4. Mediation of interlayer couplings in the [(MBT)(MnTe)$_m$]$_5$ system. a,** *m*-dependent anomalous
511 Hall curves at T = 1.5 K. All samples show the same spin-flop behavior regardless of the MnTe thickness. **b**,
512 The extracted transition field H_s is insensitive to the *m* at different temperatures. **c,** Temperature-dependent
513 H_s curve of the [(MBT)(MnTe)$_{1.25}$]$_5$ superlattice as compared with the pure 5 SL MBT control sample (*m* =
514 0). **d,** The Néel temperature T_N remains almost unchanged in all [(MBT)(MnTe)$_m$]$_5$ samples, indicating the
515 stabilization effect by the MnTe intercalation.

516

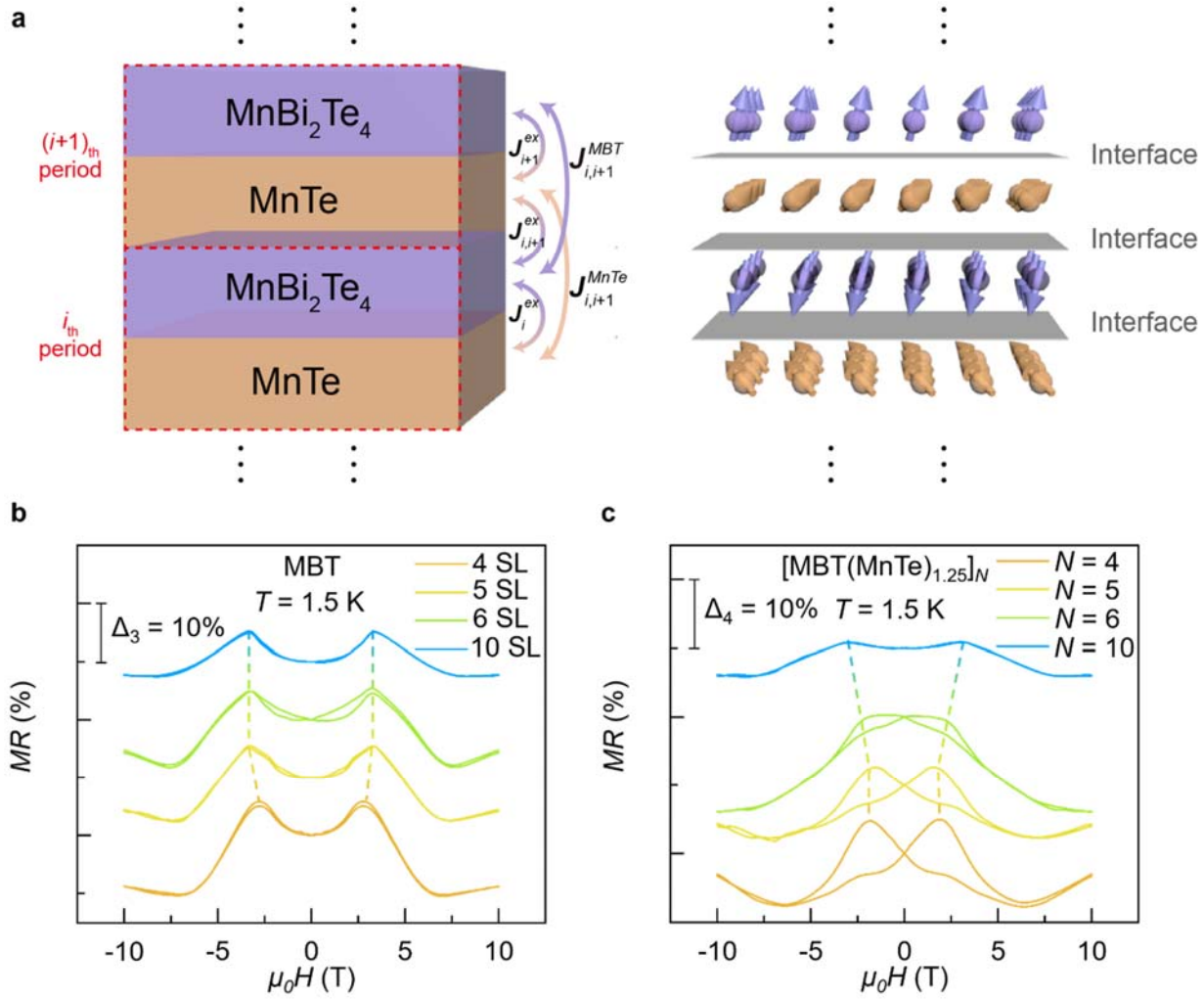

Figure 5. Tunable magneto-resistance responses through superlattice engineering. a, Illustrations of the interfacial and interlayer exchange interactions (left panel) and the resulting canted spin configuration (right panel) for the $[(MBT)(MnTe)_m]_N$ superlattices based on the modified linear chain model simulation. The in-plane spin rotation is induced by J_i^{ex}. Evolutions of MR responses in **b**, thickness-dependent pure MBT thin films and **c**, $[(MBT)(MnTe)_{1.25}]_N$ samples. With the number of superlattice repeats N increases from 4 to 10, the reinforced canted magnetization and long-range interactions drive the overall MR signal from the FM-dominated double-split butterfly shape towards the AFM-type GMR contour.